Supplement of Atmos. Chem. Phys., 26, 9657–9678, 2026
https://doi.org/10.5194/acp-26-9657-2026-supplement

Atmospheric Chemistry and Physics
Open Access

Supplement of

Aircraft-derived particle fluxes distinguish entrainment zone and decoupled layer nucleation in marine boundary layers

Ajmal Rasheeda Satheesh et al.

Correspondence to: Nicholas Meskhidze (nmeskhidze@ncsu.edu)

Time lag correction

Accurate temporal alignment between the vertical wind speed and particle concentration signals is essential for reliable flux calculations. Since the AIMMS-20 probe and the isokinetic inlet are located at different positions on the aircraft, a time lag exists between the two signals. Lag times were determined individually for each flux calculation period using covariance maximization, as described in Section 2.3.2 of the main text. This section provides the supporting validation analysis.

CPC data quality control

Periods of CPC 3772 malfunction were identified by comparing its total particle number concentration with the integral number concentration derived from FIMS size distributions over the full campaign. Because the CPC 3772 detects all particles larger than 10 nm while the FIMS range ends at 600 nm, the CPC should report values at or above the integral FIMS concentration during normal operation. The histogram of the difference between the two records (Figure S1) is accordingly peaked near zero with a positive tail, while sustained excursions into strongly negative values mark episodic instrument malfunctions, most likely associated with working fluid depletion or flow rate changes at the critical orifice. Based on this comparison, records in which the CPC concentration fell below 10% of the simultaneous FIMS concentration were flagged as physically implausible and excluded from analysis (Sect. 2.2 of the main text).

CPC synchronization validation

Both CPCs draw sample air from the same isokinetic inlet manifold. However, because each CPC detector unit is connected to the manifold via tubing of different length, the air transport time from the inlet to each detector differs (Fig. 4, Goldberger, 2020). This difference in transport time means the two CPCs may not sample identical air parcels at exactly the same moment, necessitating validation of their temporal synchronization. Figure S2 shows concentration measurements from both CPCs for a representative flight day. Despite differing absolute values, expected given their different size detection limits (3 nm vs. 10 nm), the temporal patterns closely align. To quantify this agreement, Spearman correlation coefficients (ρ) were calculated for both CPC records after removing cloud droplet shattering artifacts and excluding SPE periods, since only the ultrafine CPC detects SPEs. From the complete campaign dataset, 370 seconds of data were randomly selected to avoid selection bias, yielding a ρ of 0.97 (Fig. S3). The full CPC dataset was segmented into 20-second intervals, each corresponding to approximately 2 km of horizontal flight path, and lag times were determined for each interval using covariance maximization (Fig. S4). Lag times of 0 and −1 seconds occurred in 13% and 27% of intervals respectively. The variability in lag times arises primarily from the 1 Hz temporal resolution of the measurements: since the true lag is unlikely to be an exact integer number of seconds, it is effectively rounded to the nearest second when determined by covariance maximization, causing an apparent alternation between 0 and −1 second values. Secondary contributions may arise from minor variations in flow velocity within the inlet tubing due to changes in ambient pressure and temperature with altitude, despite active flow rate regulation. On the spatial scale, lag times of 0 and −1 seconds correspond to spatial displacements of 0–100 m at typical aircraft speeds, which is small relative to the flux-carrying eddy scales resolved in this study. No single lag time was sufficiently dominant to apply uniformly across the campaign; applying a uniform lag would therefore introduce systematic errors in the flux covariance. Sensitivity analysis confirmed that derived fluxes change by an average of less than 16% when the lag is varied by ±1 second, supporting the robustness of the individual lag determination approach.

Pressure-based validation of co-located sampling

The lag correction was independently validated by comparing pressure measured at the isokinetic inlet with static pressure measured by the Rosemount 1201F1 sensor on the AIMMS-20 probe. Since both sensors respond to the same ambient pressure field, they should be in close agreement if the instruments are sampling the same air mass. Figure S5 shows pressure time series from both sensors for a representative flight day, confirming that both records track the same pressure variations at 1 Hz resolution. Figure S6 shows the campaign-wide scatter of the two pressure records, which yields $\rho = 0.99$ and lies parallel to the 1:1 line. The systematic offset of ~50 hPa (corresponding to ~400 m of pressure altitude) is most likely attributable to an instrument artifact. The high correlation confirms that both instruments responded to the same ambient pressure field. Covariance maximization applied to the pressure records (Figure S7) again showed that no single lag time was appropriate across the full campaign, consistent with the CPC-based analysis and further supporting the use of individually determined lag times for each flux calculation period.

.

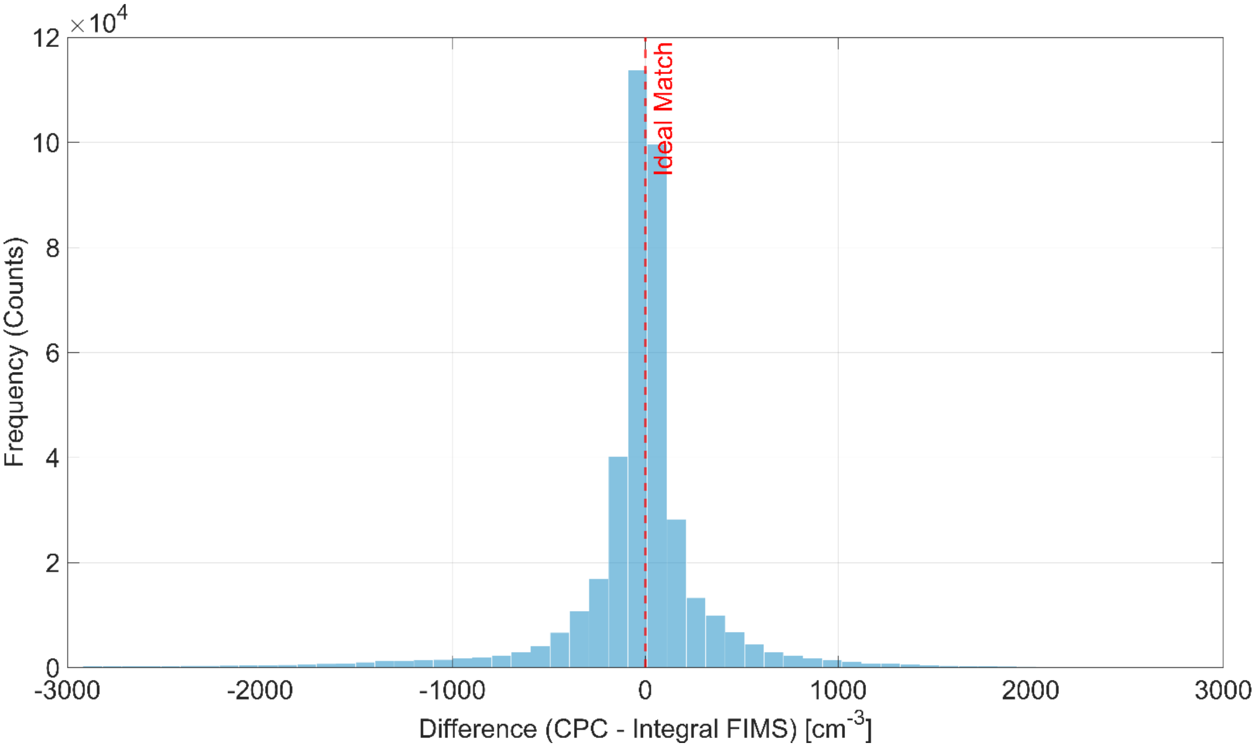

Figure S1. Histogram of the difference between total particle number concentration measured by CPC model 3772 and integral FIMS concentration (CPC – integral FIMS) across all campaign data. Positive values indicate CPC exceeding integral FIMS, as expected under normal operating conditions. Negative values reflect episodic periods of CPC malfunction used to define the 10% quality control threshold.

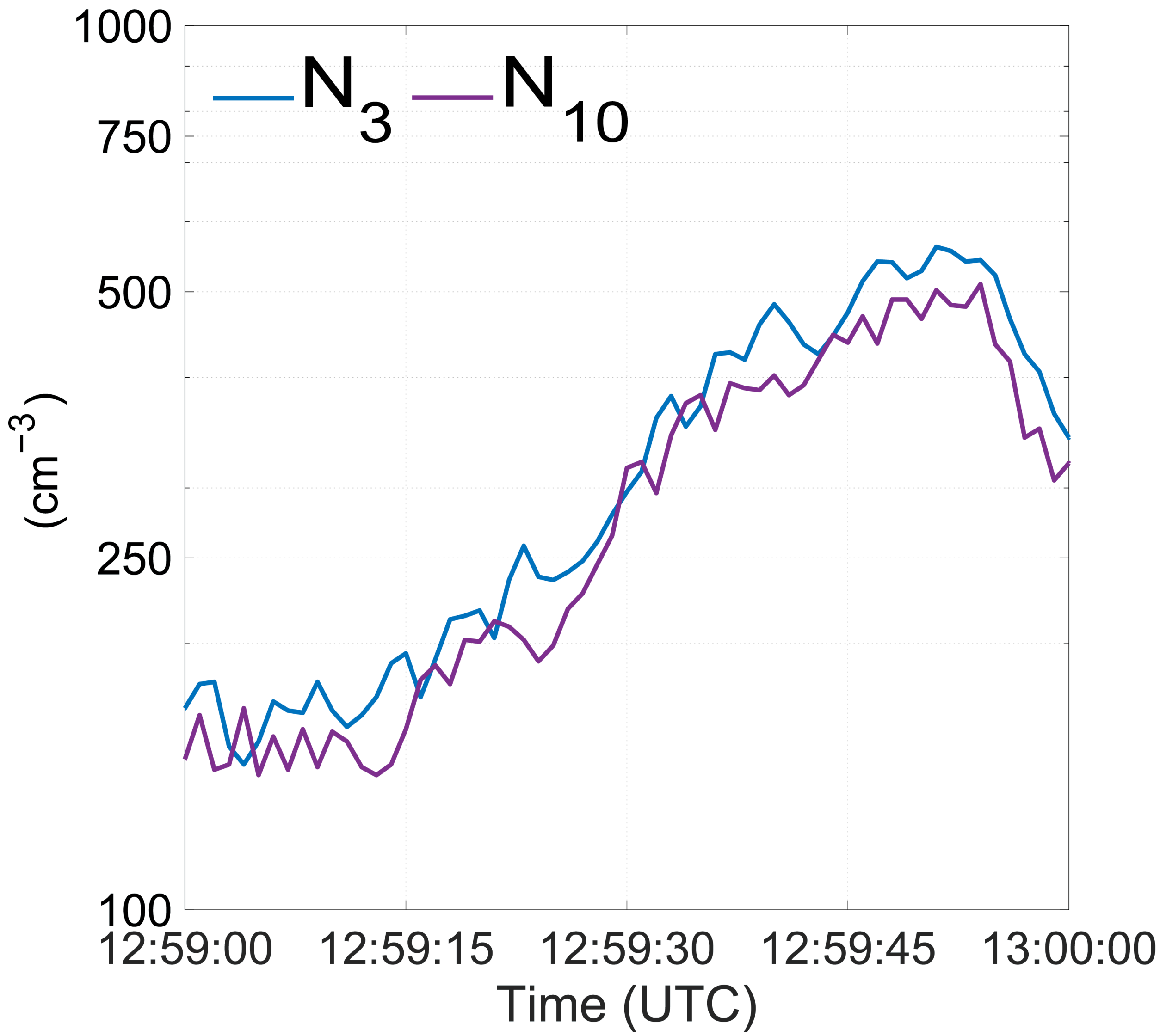

Figure S2. **Time series of particle concentration measurements from both CPCs (CPC 3025A and CPC 3772) for a representative flight day, showing that the temporal patterns closely align despite differing absolute values due to different size detection limits.**

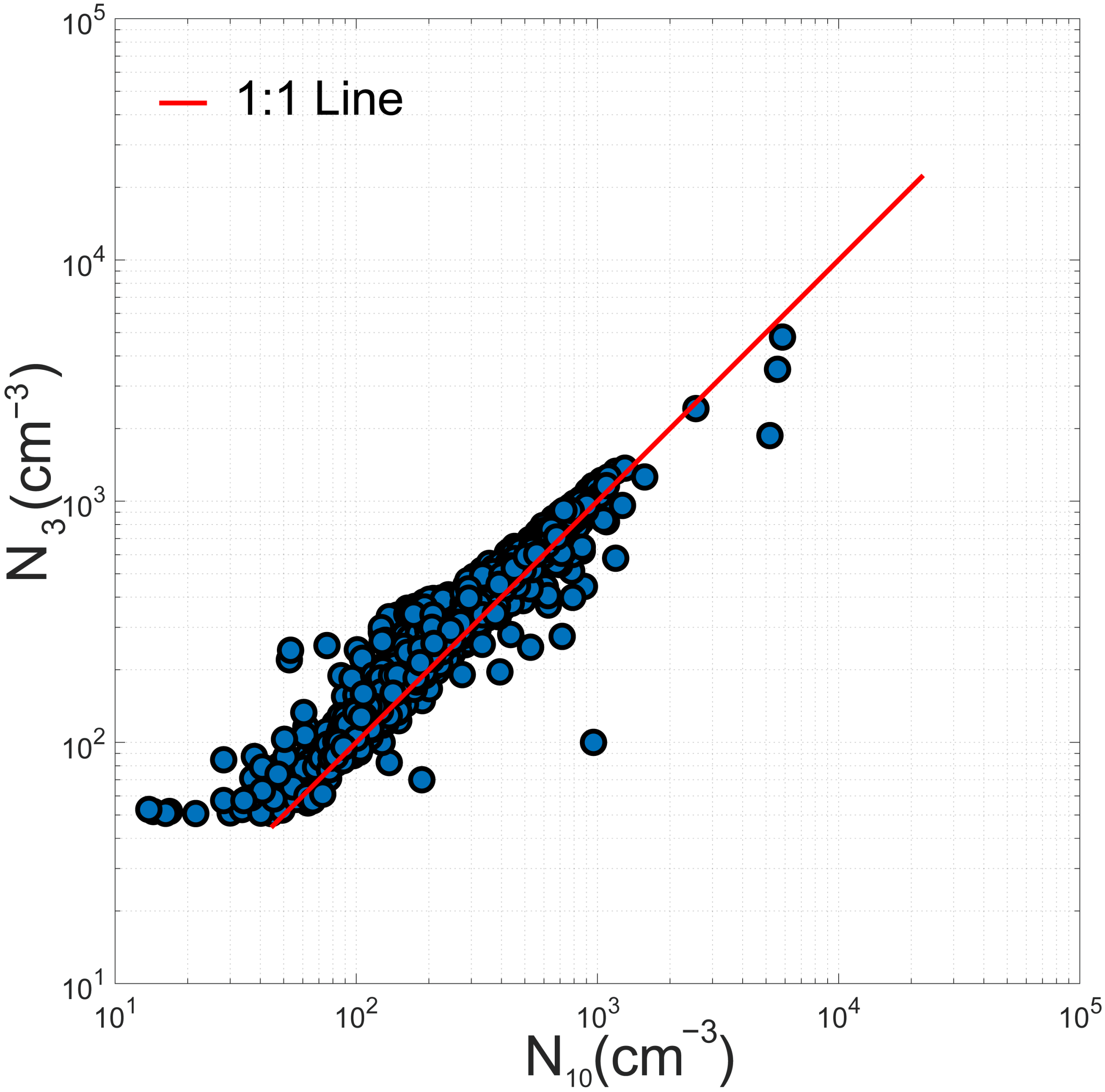

Figure S3. Scatter plot of particle number concentrations from the two CPCs (N_3 from the CPC 3025A vs. N_{10} from the CPC 3772) for the 370 randomly selected 1 s samples drawn from the full campaign dataset, after removal of cloud droplet shattering artifacts and exclusion of SPE periods. The red line denotes the 1:1 relationship. N_3 values generally equal or exceed N_{10}, as expected from the lower size detection limit of the CPC 3025A, and the two records yield a Spearman correlation coefficient of $\rho = 0.97$, confirming temporal synchronization between the instruments.

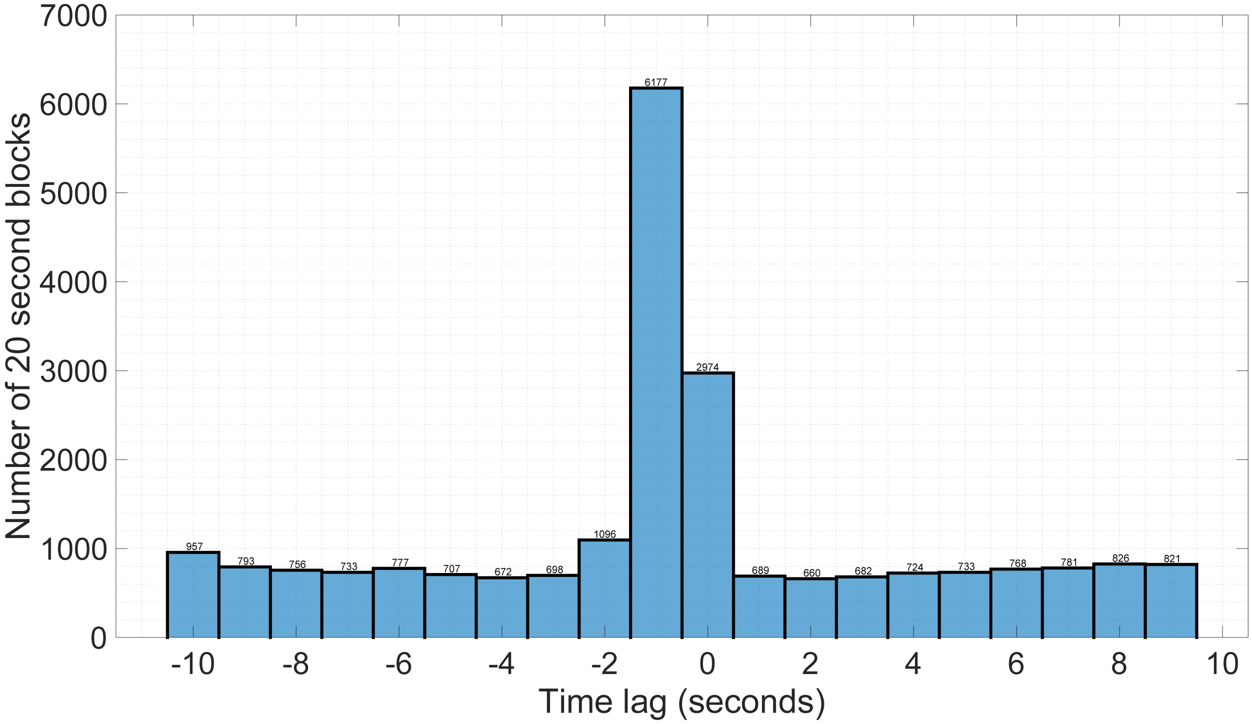

Figure S4. Distribution of lag times determined by covariance maximization across all 20-second flight segments for the entire campaign, showing that lag times of 0 and −1 seconds occurred in 13% and 27% of cases respectively, and demonstrating why no single fixed lag time was appropriate for the full campaign.

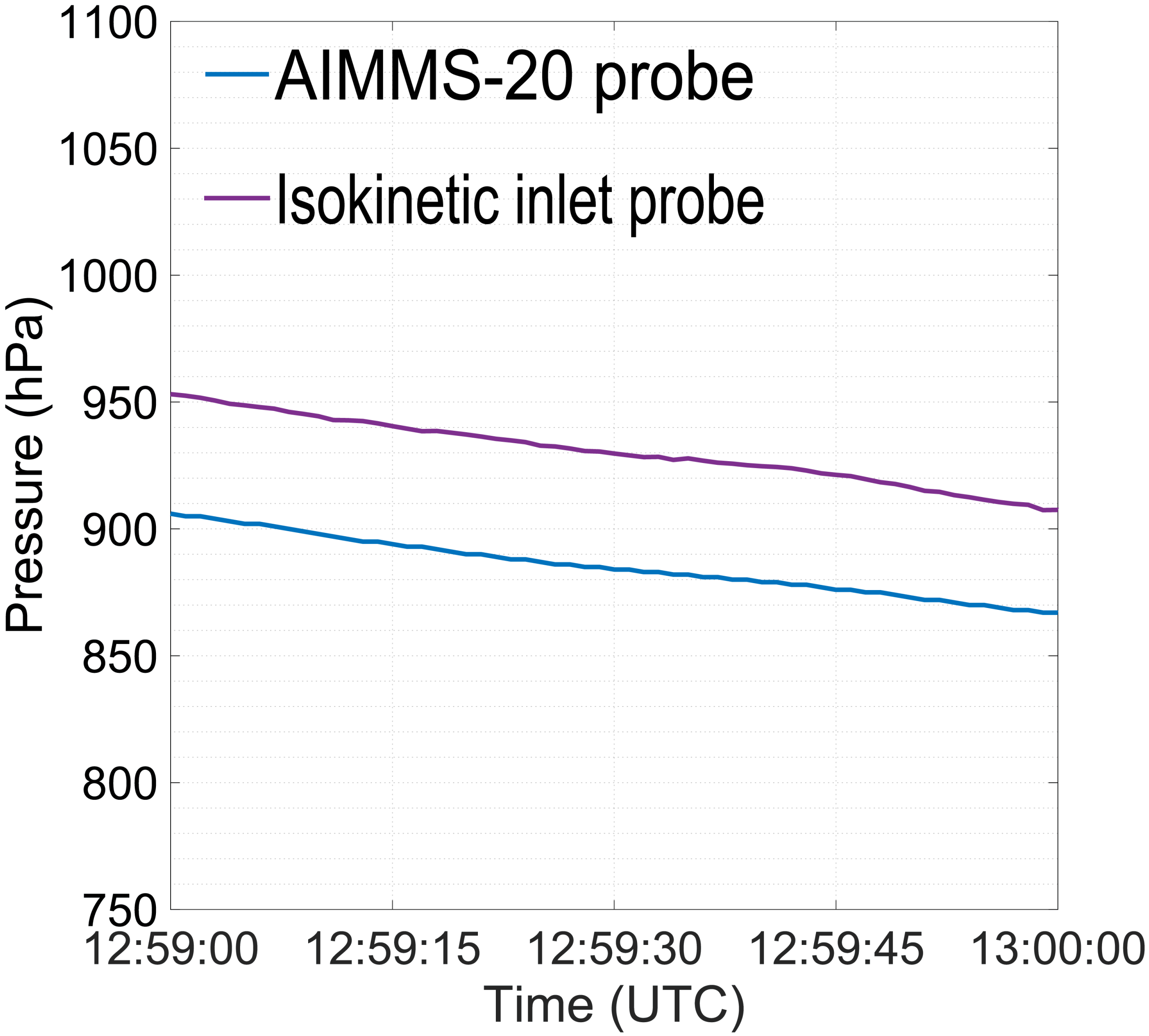

Figure S5. Time series of pressure measurements from the isokinetic inlet and the AIMMS-20 static pressure sensor for a representative flight day, demonstrating that both measurements follow similar pressure variation patterns at 1 Hz temporal resolution.

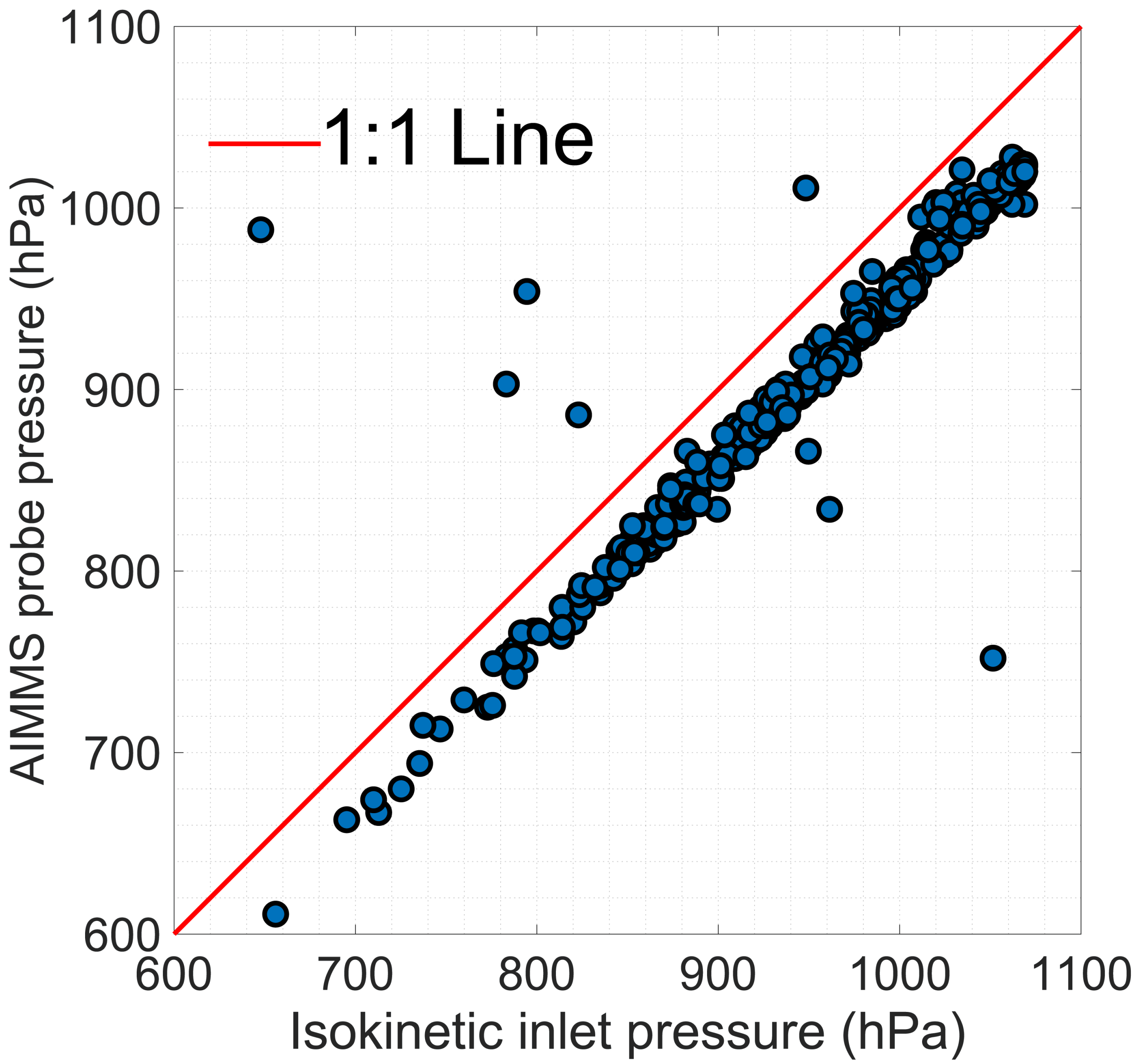

Figure S6. Scatter plot of pressure measurements from the Rosemount 1201F1 sensor attached to the AIMMS–20 probe vs those at the isokinetic inlet.

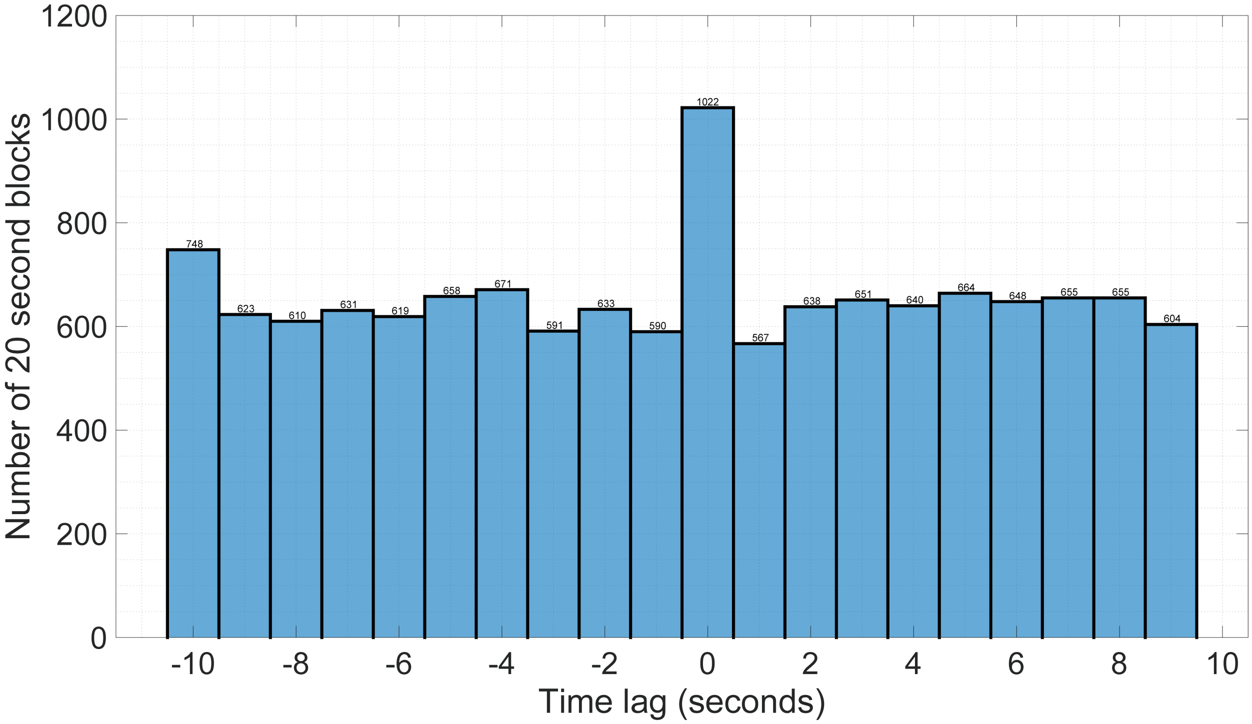

Figure S7. Frequency distribution of pressure-derived lag times across the campaign, showing consistency with the CPC-derived lag time analysis and supporting the individual lag time determination approach. Note the total data points here are different from Fig. S4, as isokinetic inlet pressure data was not always available.

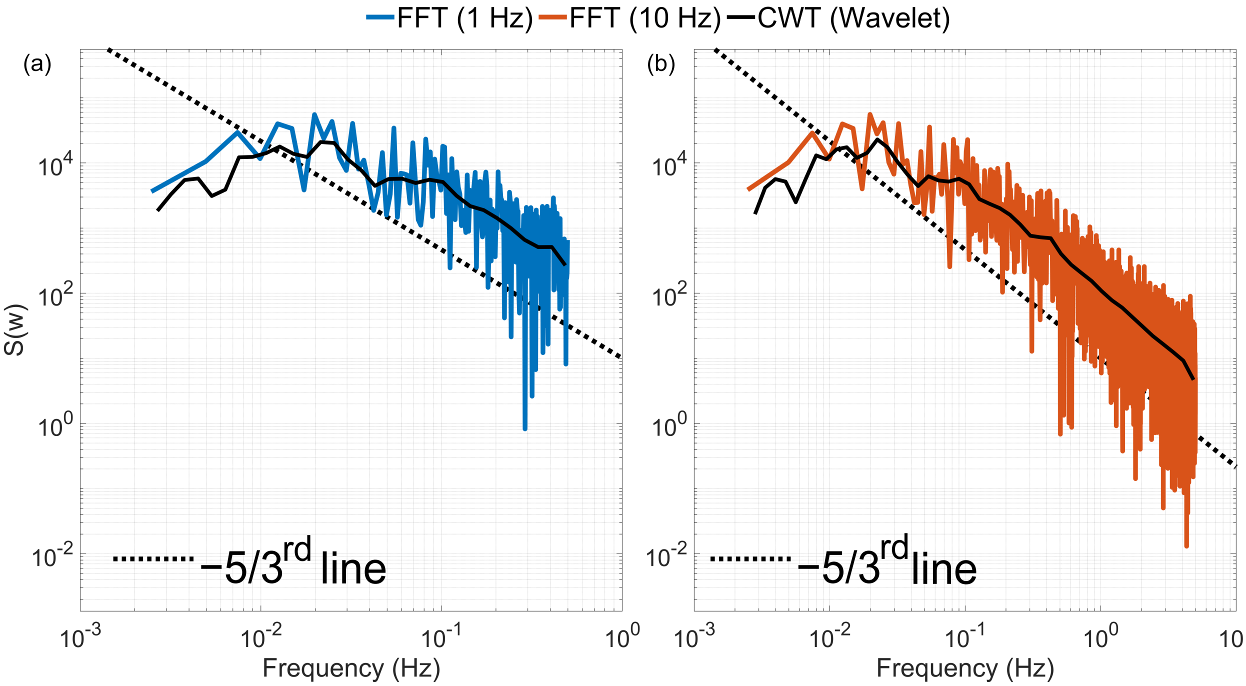

Figure S8. Power spectral density for vertical wind velocity at (a) 1 Hz and (b) 10 Hz

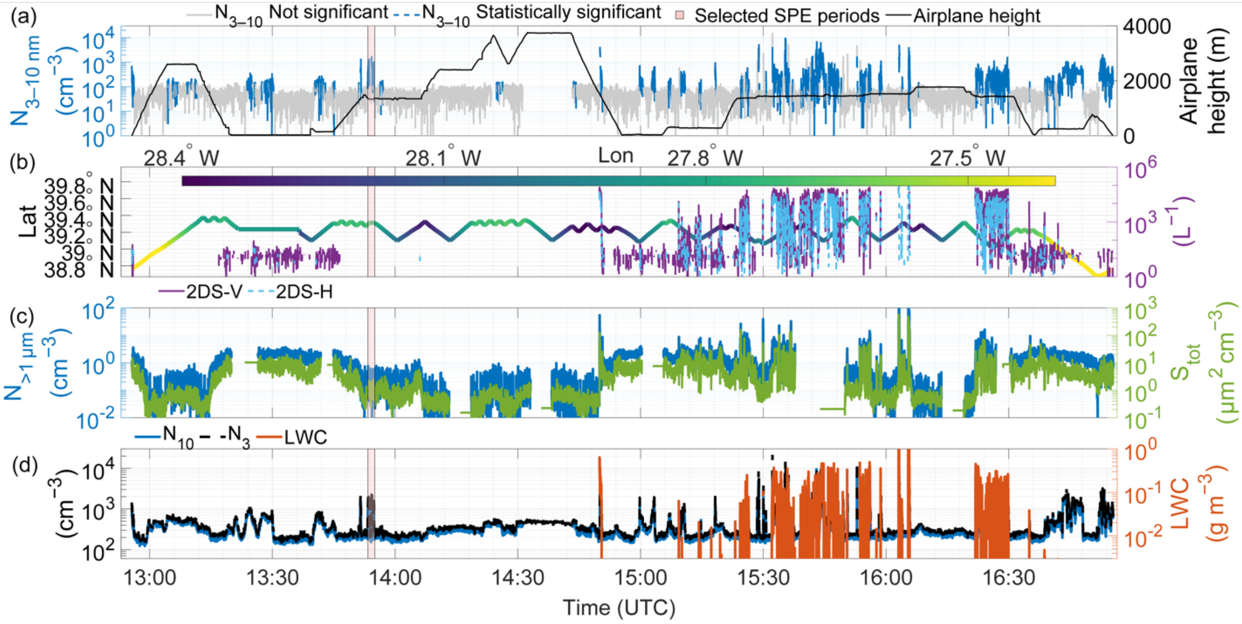

Figure S9. Multi-parameter time series analysis during the February 10, 2018 flight showing: (a) $N_{3\text{-}10}$ particle concentrations and aircraft altitude; (b) aircraft position (latitude and longitude) and drizzle number concentration; (c) supermicron particle concentration and total particle surface area (S_{tot}) (d) particle number concentrations (N_{10} and N_3) and liquid water content. Gaps in the time series indicate the missing data.

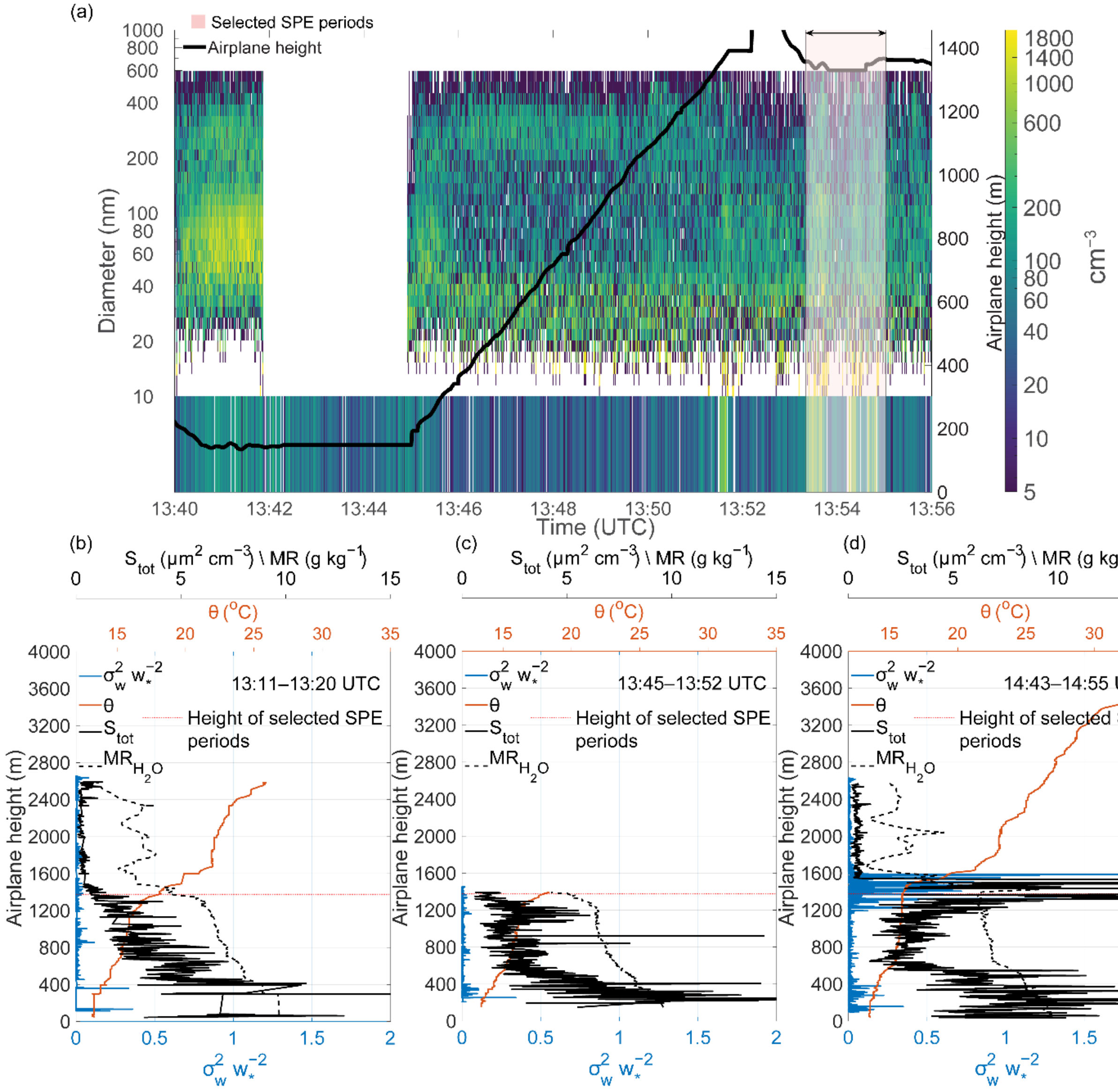

Figure S10. (a) Size-resolved particle number concentrations (10–600 nm) from FIMS as a function of time and altitude, with N_{3-10} concentrations shown in the lower strip. Pink shading indicates selected SPE periods. (b-d) Vertical profiles of potential temperature (θ), normalized vertical velocity variance ($\sigma_w^2\, w_*^{-2}$), total particle surface area (S_{tot}), and water vapor mixing ratio (MR_{H2O}) for three time periods nearest to the selected SPE periods: (b) 13:11–13:20 UTC, (c) 13:45–13:52 UTC, and (d) 14:43–14:55 UTC. Gaps in the time series indicate the missing data.

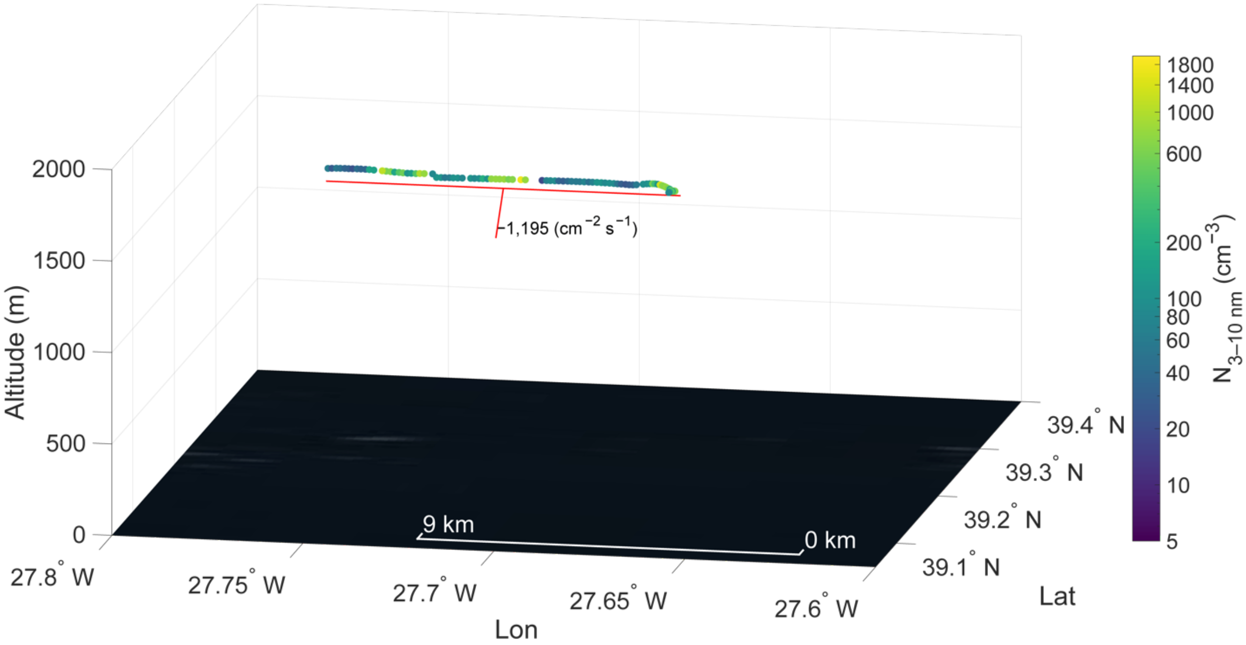

Figure S11. Spatial distribution of $N_{3\text{-}10}$ particle concentrations along the flight track at ~1375 m altitude during the period highlighted in Figures S9 and S10. Calculated vertical turbulent fluxes are labeled at their respective measurement locations. Color scale indicates $N_{3–10}$ particle number concentrations (cm^{-3}). The background shows a true-color satellite-corrected reflectance image from the overpass at 14:25 UTC, with the ocean surface appearing dark and clouds appearing white, Credit: NASA Worldview Snapshots.

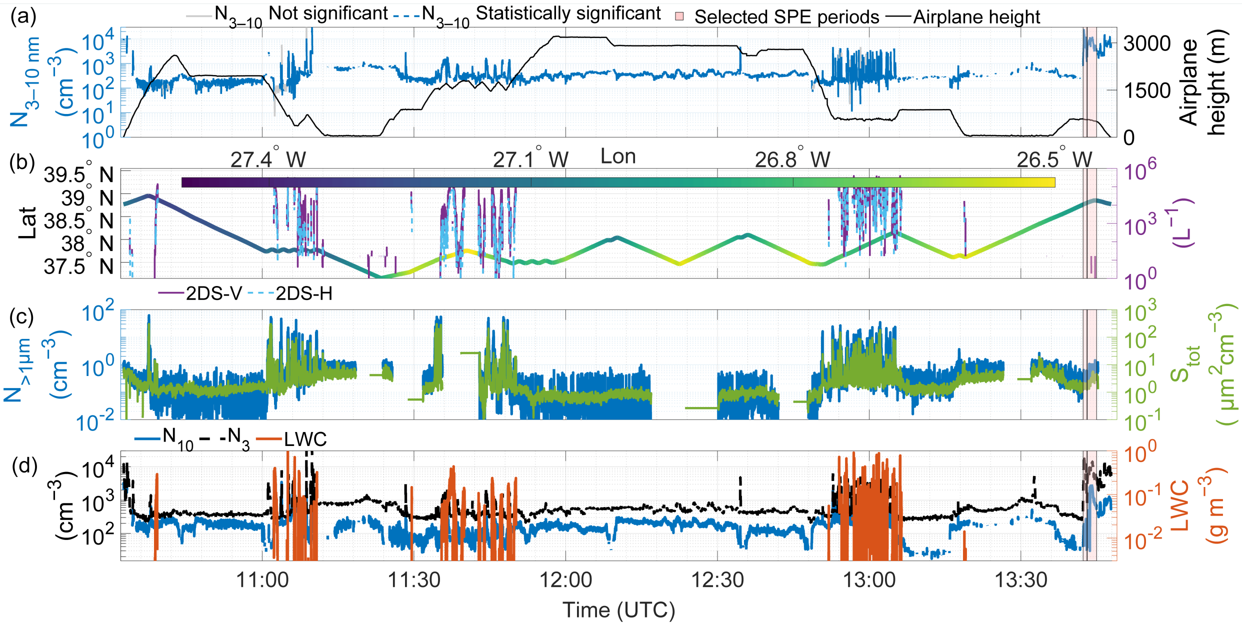

Figure S12. Multi-parameter time series analysis during the July 07, 2017 flight showing: (a) $N_{3\text{-}10}$ particle concentrations and aircraft altitude; (b) aircraft position (latitude and longitude) and drizzle number concentration; (c) supermicron particle concentration and total particle surface area (S_{tot}) (d) particle number concentrations (N_{10} and N_3) and liquid water content. Gaps in the time series indicate the missing data.

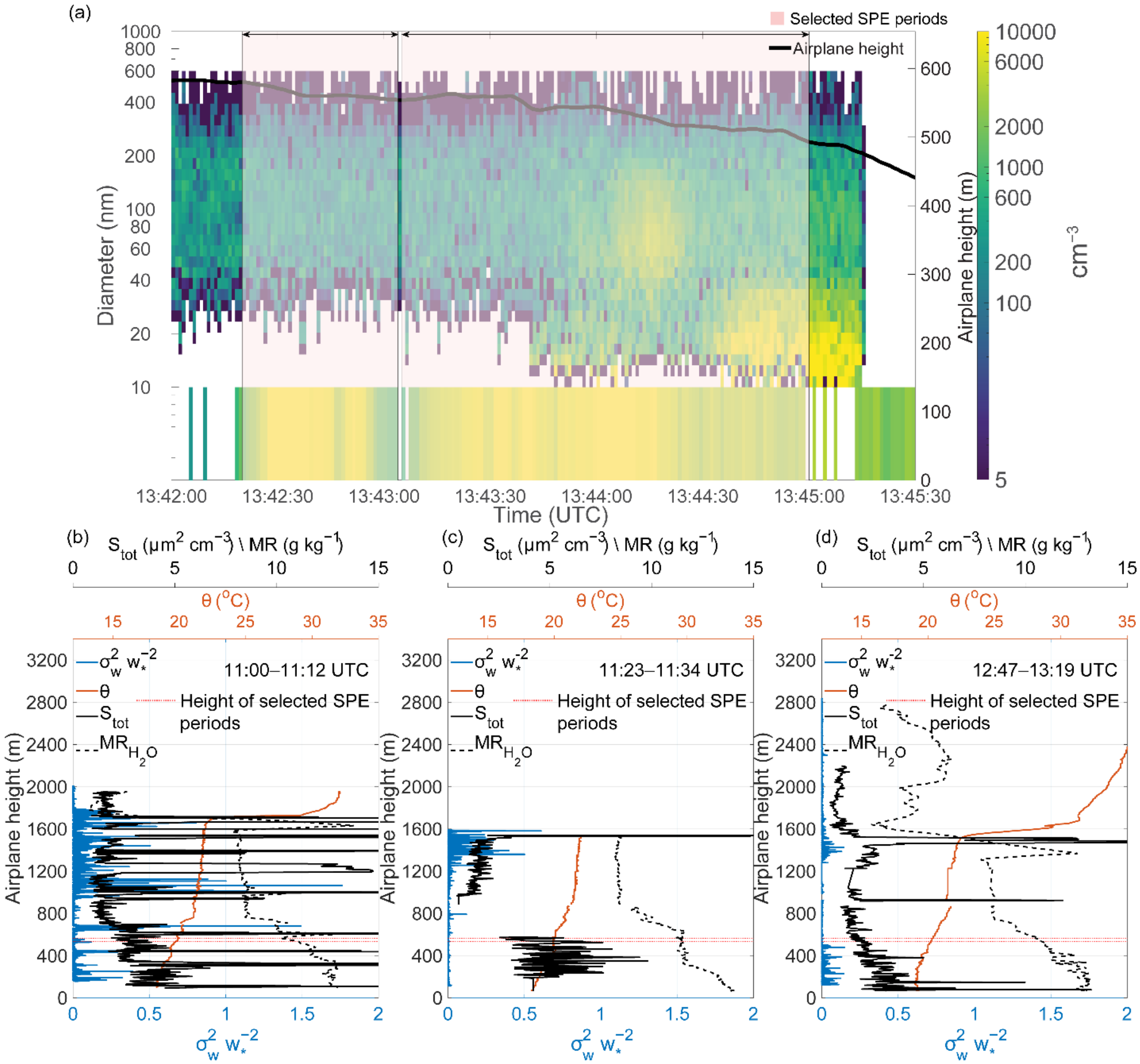

Figure S13. (a) Size-resolved particle number concentrations (10–600 nm) from FIMS as a function of time and altitude, with $N_{3\text{–}10}$ concentrations shown in the lower strip. Pink shading indicates selected SPE periods. (b-d) Vertical profiles of potential temperature (θ), normalized vertical velocity variance ($\sigma_w^2\ w_*^{-2}$), total particle surface area (S_{tot}), and water vapor mixing ratio (MR_{H2O}) for three time periods nearest to the selected SPE periods: (b) 11:00–11:12 UTC, (c) 11:23–11:34 UTC, and (d) 12:47–13:19 UTC. Gaps in the time series indicate the missing data.

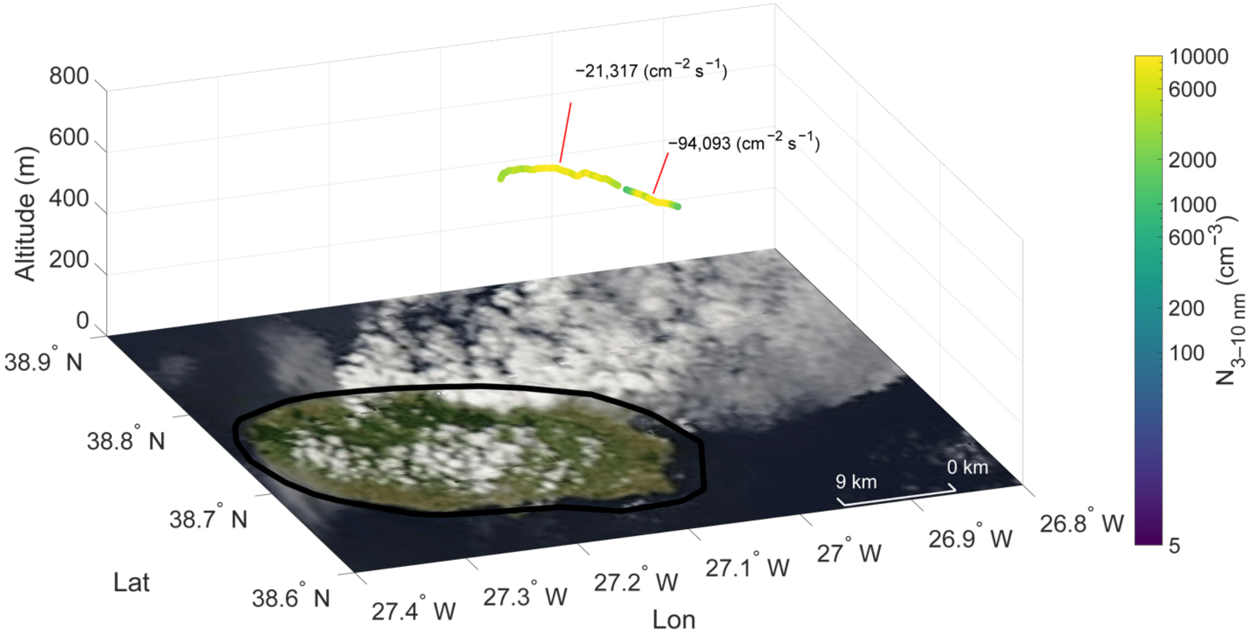

Figure S14. Spatial distribution of $N_{3–10}$ particle concentrations along the flight track at ~550 m altitude during the period highlighted in Figures S12 and S13. Calculated vertical turbulent fluxes are labeled at their respective measurement locations. Color scale indicates $N_{3–10}$ particle number concentrations (cm^{-3}). The background shows a true-color satellite-corrected reflectance image from the overpass at 15:02 UTC with the ocean surface appearing dark and clouds appearing white, Credit: NASA Worldview Snapshots.

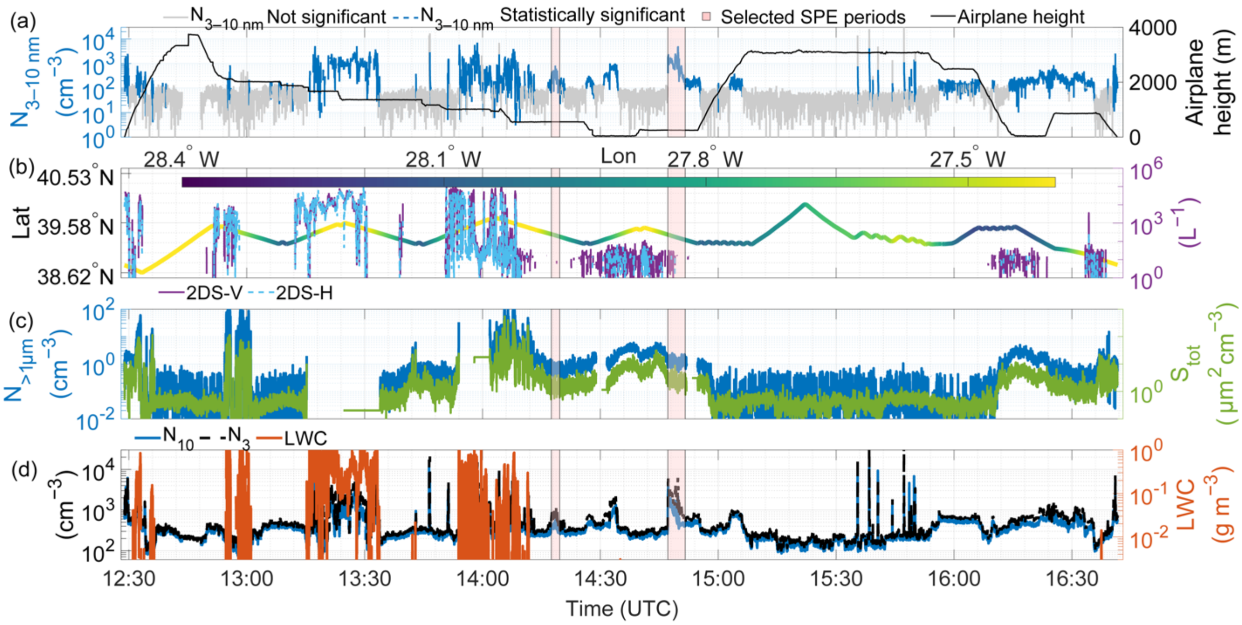

Figure S15. Multi–parameter time series analysis during the February 18, 2018 flight showing: (a) $N_{3\text{-}10}$ particle concentrations and aircraft altitude; (b) aircraft position (latitude and longitude) and drizzle number concentration; (c) supermicron particle concentration and total particle surface area (S_{tot}) (d) particle number concentrations (N_{10} and N_3) and liquid water content. Gaps in the time series indicate the missing data.

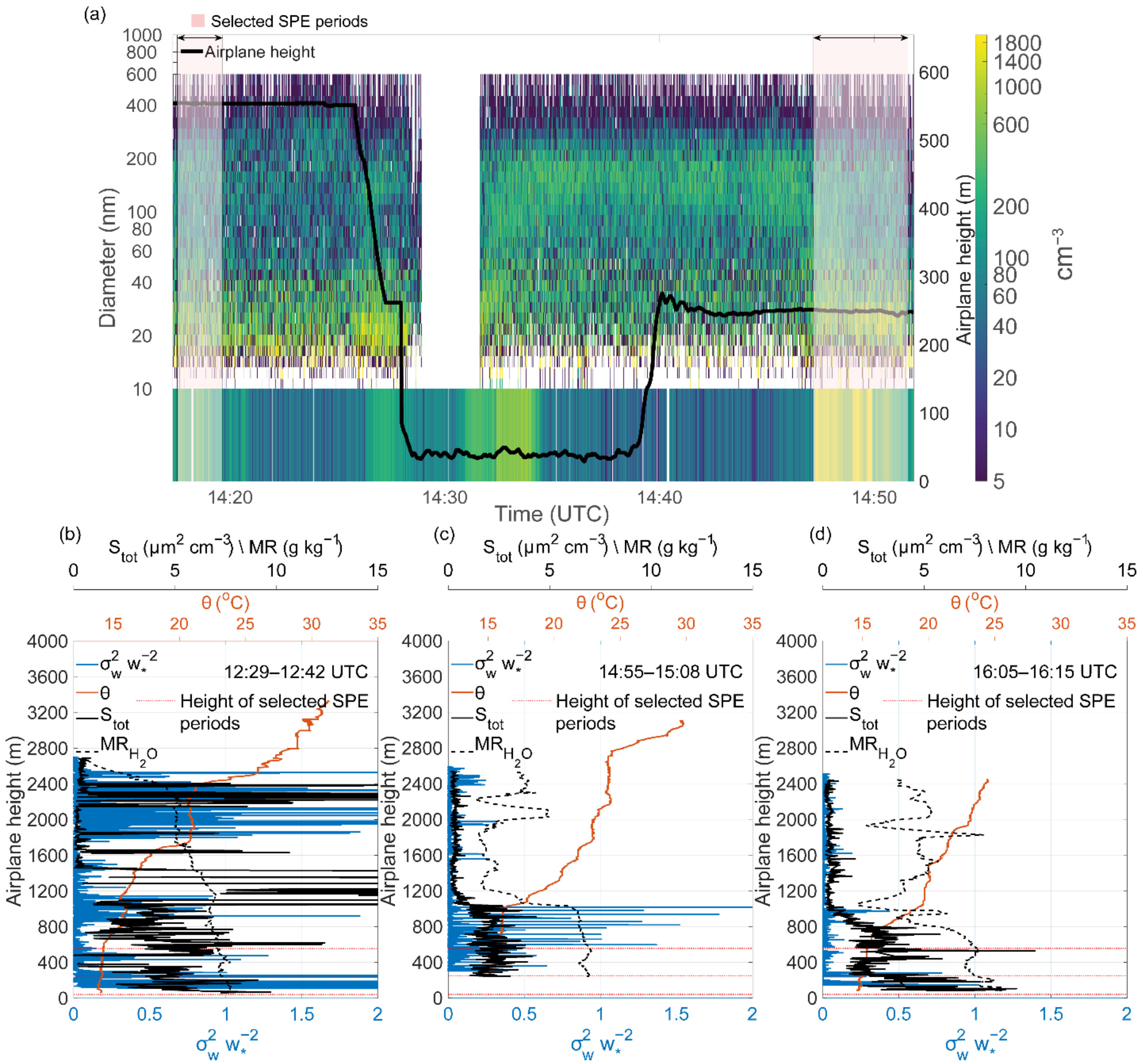

Figure S16. (a) Size-resolved particle number concentrations (10–600 nm) from FIMS as a function of time and altitude, with $N_{3–10}$ concentrations shown in the lower strip. Pink shading indicates selected SPE periods. (b-d) Vertical profiles of potential temperature (θ), normalized vertical velocity variance ($\sigma_w^2\ w_*^{-2}$), total particle surface area (S_{tot}), and water vapor mixing ratio (MR_{H2O}) for three time periods nearest to the selected SPE periods: (b) 12:29–12:42 UTC, (c) 14:55–15:08 UTC, and (d) 16:05–16:15 UTC. Gaps in the time series indicate the missing data.

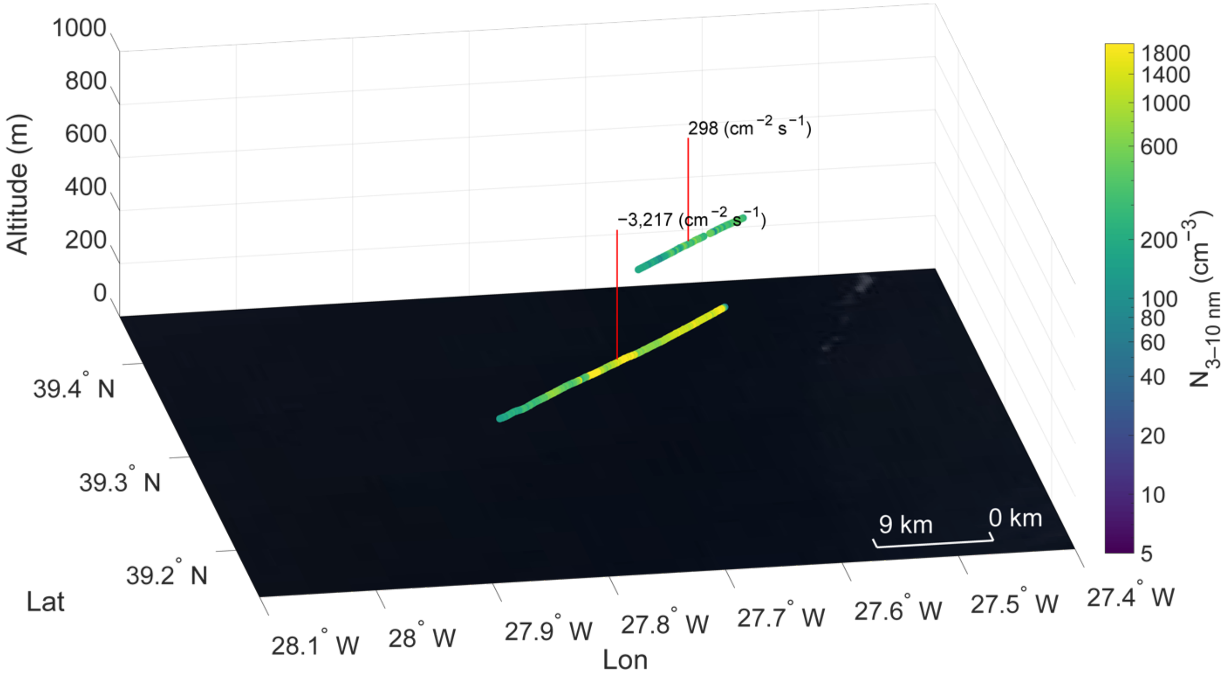

Figure S17. Spatial distribution of N_{3-10} particle concentrations along the flight track at ~550 m and 250 m altitude respectively during the period highlighted in pink in Figures S15 and S16. Calculated vertical turbulent fluxes are labeled at their respective measurement locations. Color scale indicates N_{3-10} particle number concentrations (cm^{-3}). The background shows a true-color satellite-corrected reflectance image from the overpass at 14:50 UTC with the ocean surface appearing dark and clouds appearing white, Credit: NASA Worldview Snapshots.

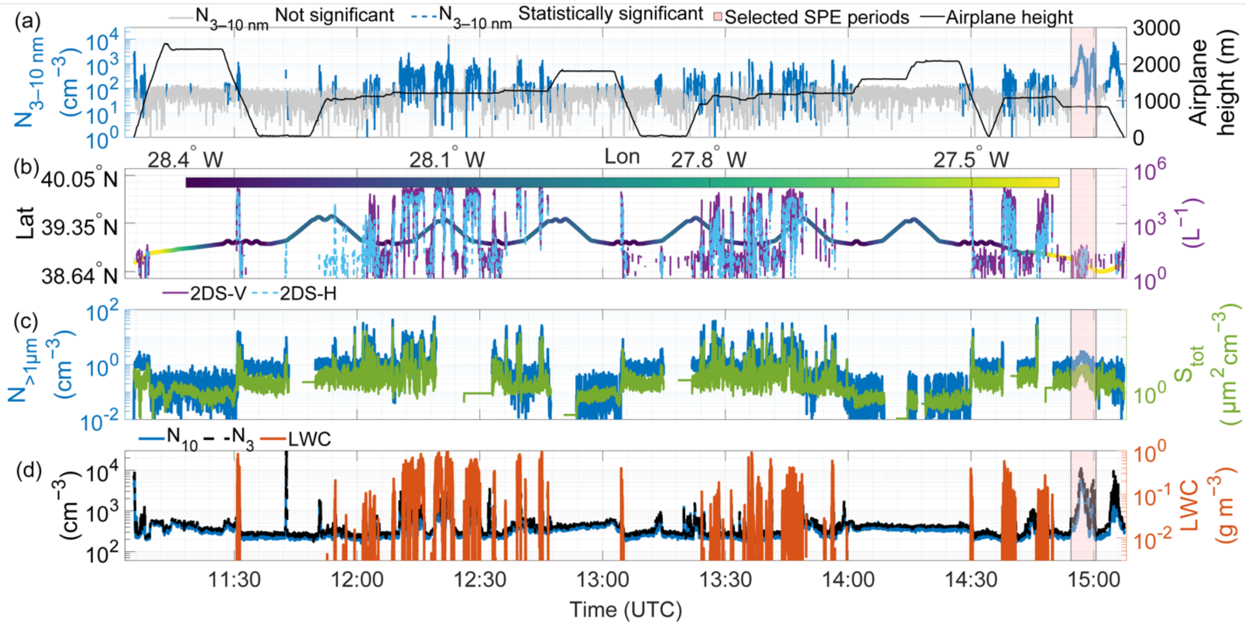

Figure S18. Multi–parameter time series analysis during the February 12, 2018 flight showing: (a) $N_{3\text{-}10}$ particle concentrations and aircraft altitude; (b) aircraft position (latitude and longitude) and drizzle number concentration; (c) supermicron particle concentration and total particle surface area (S_{tot}) (d) particle number concentrations (N_{10} and N_3) and liquid water content. Gaps in the time series indicate the missing data.

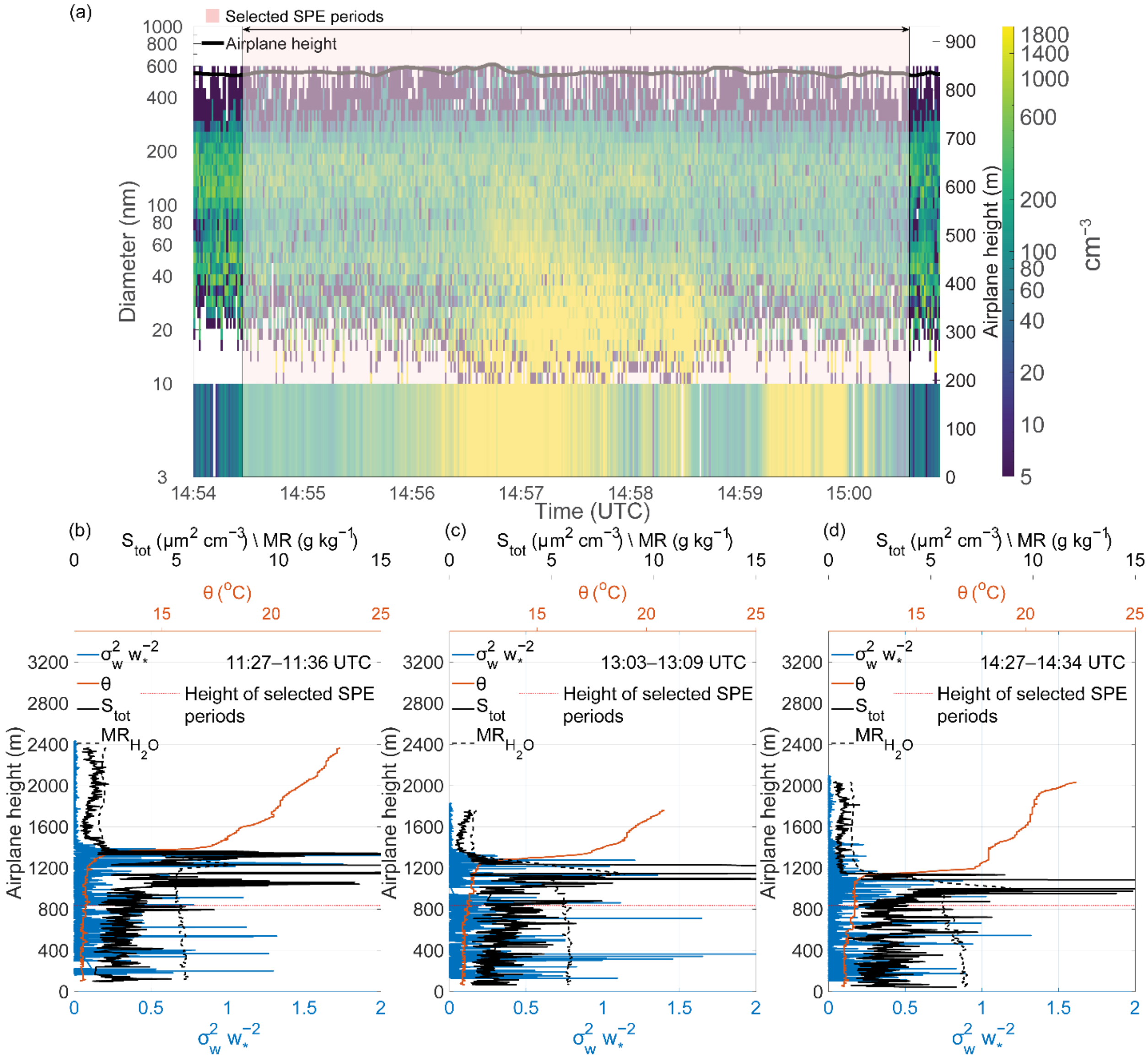

Figure S19. (a) Size-resolved particle number concentrations (10–600 nm) from FIMS as a function of time and altitude, with $N_{3\text{–}10}$ concentrations shown in the lower strip. Pink shading indicates selected SPE periods. (b-d) Vertical profiles of potential temperature (θ), normalized vertical velocity variance ($\sigma_w^2\, w_*^{-2}$), total particle surface area (S_{tot}), and water vapor mixing ratio (MR_{H2O}) for three time periods nearest to the selected SPE periods: (b) 11:27–11:36 UTC, (c) 13:03–13:09 UTC, and (d) 14:27–14:34 UTC. Gaps in the time series indicate the missing data.

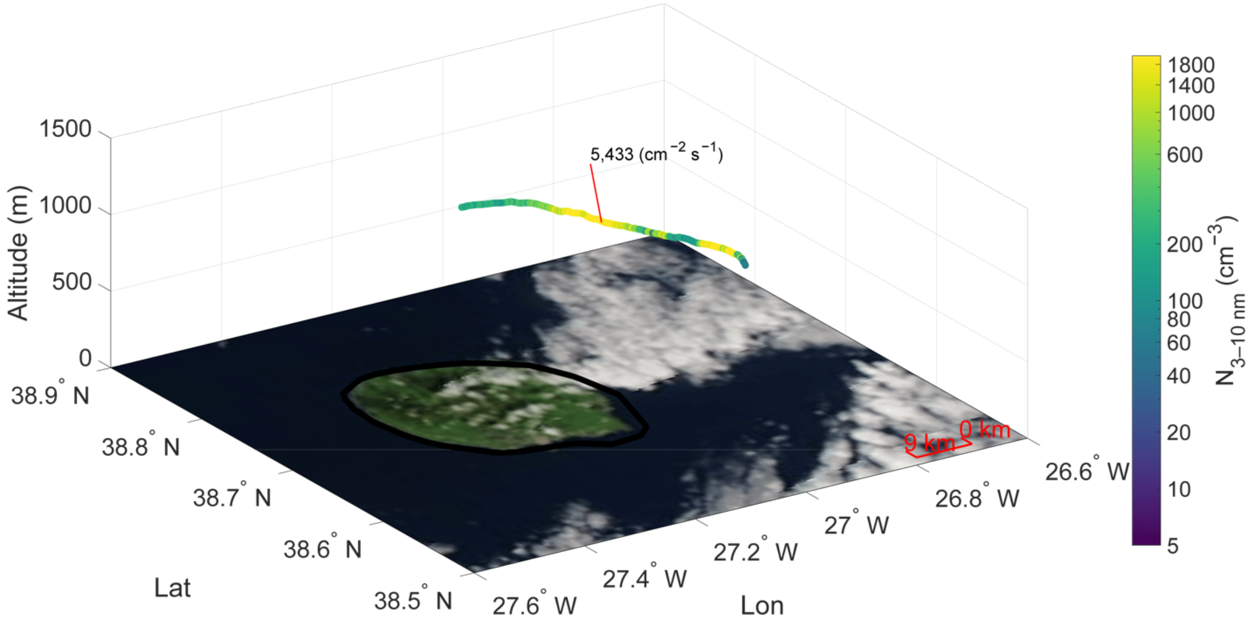

Figure S20. Spatial distribution of N_{3-10} particle concentrations along the flight track at ~830 m altitude during the period highlighted in Figures S18 and S19. Calculated vertical turbulent fluxes are labeled at their respective measurement locations. Color scale indicates N_{3-10} particle number concentrations (cm^{-3}). The background shows a true-color satellite-corrected reflectance image from the overpass at 15:27 UTC, with the ocean surface appearing dark and clouds appearing white, Credit: NASA Worldview Snapshots.